Article

Structure

Structural analysis of the architecture and *in situ* localization of the main S-layer complex in *Deinococcus radiodurans*

Graphical abstract

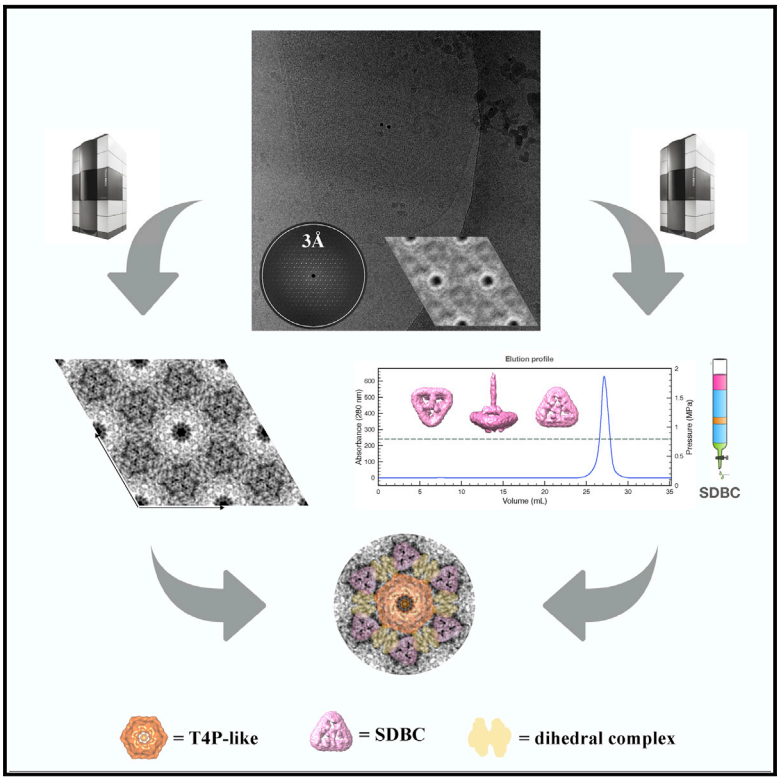

Highlights

- Projection map of a native S-layer at 4.5-Å resolution by cryo-EC
- SDBC structure at 11-Å resolution by cryo-EM single-particle analysis
- SDBC *in situ* localization and orientation
- S-layer as a stabilizing component of cell-wall status

Authors

Domenica Farci, Sami Kereïche, Sushil Pangeni, ..., Matteo Ceccarelli, Mathias Winterhalter, Dario Piano

Correspondence

domenica_farci@sggw.edu.pl (D.F.), sami.kereiche@lf1.cuni.cz (S.K.), dario.piano@unica.it (D.P.)

In brief

Deinococcus radiodurans is an extremophile whose main S-layer complex provides specific resistance properties. Farci et al. describe the organization and *in situ* localization of the S-layer by cryo-electron microscopy. Unique features of the main protein complex and its connection to underlying membranes are presented.

Farci et al., 2021, Structure *29*, 1279–1285
November 4, 2021
https://doi.org/10.1016/j.str.2021.06.014

CellPress

Structure

CellPress

Article

Structural analysis of the architecture and *in situ* localization of the main S-layer complex in *Deinococcus radiodurans*

Domenica Farci,[1,*] Sami Kereïche,[2,*] Sushil Pangeni,[3] Patrycja Haniewicz,[1] Igor V. Bodrenko,[4] Matteo Ceccarelli,[4] Mathias Winterhalter,[3] and Dario Piano[1,5,6,*]

[1]Department of Plant Physiology, Warsaw University of Life Sciences – SGGW, 02-776 Warsaw, Poland
[2]Institute of Biology and Medical Genetics, First Faculty of Medicine, Charles University, 12800 Prague, Czech Republic
[3]Department of Life Sciences & Chemistry, Jacobs University Bremen, 28759 Bremen, Germany
[4]Department of Physics and IOM/CNR, University of Cagliari, 09042 Monserrato, Italy
[5]Laboratory of Plant Physiology and Photobiology, Department of Life and Environmental Sciences, University of Cagliari, 09123 Cagliari, Italy
[6]Lead contact
*Correspondence: domenica_farci@sggw.edu.pl (D.F.), sami.kereiche@lf1.cuni.cz (S.K.), dario.piano@unica.it (D.P.)
https://doi.org/10.1016/j.str.2021.06.014

SUMMARY

Bacterial surface layers are paracrystalline assemblies of proteins that provide the first line of defense against environmental shocks. Here, we report the 3D structure, *in situ* localization, and orientation of the S-layer deinoxanthin-binding complex (SDBC), a hetero-oligomeric assembly of proteins that in *Deinococcus radiodurans* represents the main S-layer unit. The SDBC is resolved at 11-Å resolution by single-particle analysis, while its *in situ* localization is determined by cryo-electron crystallography on intact cell-wall fragments leading to a projection map at 4.5-Å resolution. The SDBC exhibits a triangular base with three comma-shaped pores, and a stalk departing orthogonally from the center of the base and oriented toward the intracellular space. Combining state-of-the-art techniques, results show the organization of this S-layer and its connection within the underlying membranes, demonstrating the potential for applications from nanotechnologies to medicine.

INTRODUCTION

Surface layers (S-layers) are highly ordered multi-proteinaceous coats forming the outermost envelope of many prokaryotes (Sleytr and Glauert, 1975; Sleytr, 1978; Messner and Sleytr, 1991; Sleytr et al., 1993; Bahl et al., 1997; Messner et al., 1997; Pavkov et al., 2008). The S-layer is often present in Bacteria and Archaea, carrying resistance to extreme conditions (Gentner and Mitchel, 1975; Sleytr and Sàra, 1997; Pavkov-Keller et al., 2011; Farci et al., 2016, 2018; Kumar et al., 2021), and plays essential roles in providing primary cell properties such as rigidity, adhesion, and shape (Sleytr et al., 1993; Beveridge et al., 1997; Rachel et al., 1997; Fagan and Fairweather, 2014). Despite their potentials in areas that span from biomedicine to nanotechnology (Hall et al., 2001; Mark et al., 2006; Farci et al., 2017), insights into the molecular arrangements occurring between the S-layer and the underlying cell wall are still limited. With the exception of previous pioneering studies (Baranova et al., 2012; Bharat et al., 2017), an extended structural characterization of these proteins and their S-layers at subnanometer resolution has been extremely difficult, especially due to their self-assembly properties and related tendency to aggregate (Pum et al., 2013). To date, S-layer structures and functions remain cryptic. The primary reason for this are their poorly conserved primary sequences with the only exception being the S-layer homology domain (SLH), which is extensively shared among S-layer-carrying bacteria (Sára and Sleytr, 2000). This fact has limited significantly our general overview of S-layers and makes comparative analysis meaningful only for intra-genus studies.

Since its discovery in 1956 (Anderson et al., 1956), the radioresistant bacterium *Deinococcus radiodurans* has been a model organism for S-layer studies. Several structural techniques, such as atomic force microscopy, electron crystallography, and scanning transmission electron microscopy, were applied to the study of this S-layer. These studies showed the typical six-fold symmetry of this S-layer (Baumeister et al.,1982, 1986; Rachel et al., 1986; Peters and Baumeister, 1986; Müller et al., 1996, 1997; Lister and Pinhero, 2001) and suggested it to be composed of a single polypeptide assembled into a hexagonal plane on the outer membrane surface, namely the hexagonally packed intermediate (HPI) (Baumeister et al., 1986). However, during the last decade, the S-layer of this bacterium has been extensively studied, challenging the previous suggestion of a mono-proteinaceous organization (Farci et al., 2014). These studies identified a dozen proteins involved in the articulated paracrystalline order of the S-layer (Farci et al., 2014) and

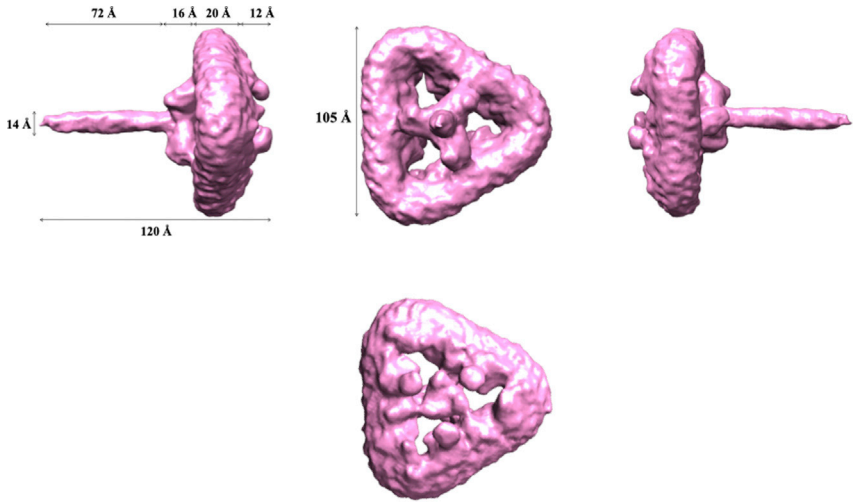

Figure 1. SDBC 3D structure and dimensions
The SDBC has a triangular shape with a needle-like structure departing orthogonally from the particle plane, the stalk. The stalk sits on a pedestal that makes the particle asymmetric; the main body shows a triangular shape with a septum departing from the center of each side and converging at the center of the particle according to a triskelion motif delimitating three comma-shaped pores. The main dimensions are indicated.

allocated them into at least two specific hetero-oligomeric complexes, the S-layer deinoxanthin-binding complex (SDBC), accounting for the interpore region of this S-layer (Farci et al., 2016), and a type IV-like piliation system, accounting for the pore region (Farci et al., 2014). Among these complexes, the main one, the SDBC, was broadly characterized both functionally and biochemically (Farci et al., 2015, 2016, 2018, 2019; Rothfuss et al., 2006; Ott et al., 2019a, 2019b; Lim et al., 2019; Adamec et al., 2020), but only recently have some of its structural features been disclosed (Farci et al., 2020).

The main SDBC component is the protein DR_2577, also known as SlpA (Farci et al., 2014). DR_2577 is a lipoprotein directly attached to the outer membrane by the SLH domain (Bahl et al., 1997; Messner et al., 1997; Pavkov et al., 2008). Being a binding site of the carotenoid deinoxanthin in the S-layer (Farci et al., 2016), the DR_2577 gives the typical color and name of "pink envelopes" to the isolated cell-wall fragments (Baumeister et al.,1982, 1986). The assembly of several copies of DR_2577 and another five proteins, namely DR_2310, DR_0505, DR_A0281, DR_A0282, and DR_A0283, results in the SDBC, which provides protection against UV radiation (Farci et al., 2016, 2018) and shows gating properties by allowing ion currents across the cell wall (Farci et al., 2020).

Here, we report the structure of the SDBC solved at 11-Å resolution by cryo-electron microscopy (cryo-EM) single-particle analysis (SPA). Furthermore, to define the *in situ* localization and orientation of the SDBC, we obtained a projection map of the cell-wall fragments at 4.5-Å resolution via cryo-electron crystallography (cryo-EC) by exploiting the natural S-layer paracrystallinity and diffraction properties. The projection map shows three complexes, the SDBC and a type IV-like piliation system, characteristic for this S-layer, and a so far unknown third complex with an apparent dihedral symmetry. For the first time cryo-EM in its diverse applications has been successfully applied to solve the structure of a main S-layer component, define its *in situ* localization, and decipher the supramolecular architecture of the whole S-layer. Therefore, here we present direct evidence for the extraordinary complexity of this S-layer and provide pivotal elements for our general understanding of these structures, combining state-of-the-art techniques in an unusual but effective pipeline.

S-layers are widespread structures among bacteria, giving protective and adhesive functions, and play a pivotal role in the pathogenesis of highly infectious species such as *Bacillus anthracis*, *Clostridium difficile*, and many others. Therefore, the present findings may help to boost the research on S-layers for possible biotechnological applications spanning from biomedicine, as antibiotic targets, to nanotechnology, exploiting their properties of self-assembling functionalized structures.

RESULTS

The SDBC is a three-channel porin with triangular shape and a stalk inserted into the membranes

The SDBC is a main S-layer unit in *D. radiodurans* and is a hetero-oligomeric complex that shows peculiar porin-like properties (Farci et al., 2020). To define the SDBC organization into the S-layer, we have isolated both the complex and the intact cell walls in their native conditions. The SDBC structure was solved by cryo-EM SPA, and its localization was identified by cryo-EC on intact cell walls.

The dataset, consisting of 11,086 particles from 1,573 micrographs, allowed us to solve a ~11-Å resolution three-dimensional (3D) model of the SDBC by SPA (EMD-12169; Figures 1, S1, and S2), with an approximated molecular mass of ~967 kDa.

With no imposed symmetry, the complex presents a triangular shape (Figure S2) with a side length of 105 Å and a height of 120 Å (Figure 1). From each of the three sides departs a septum converging with the others at the center of the particle in a triskelion fashion. The septa define three characteristic comma-shaped pores of 20 Å at the longer side (Figure 1). These septa merge in the center of the particle via a needle-like structure, hereafter referred as the stalk (Figure 1). The stalk is orthogonal to the main plane of the particle (Figure 1), and has a diameter of 14 Å and a length of 72 Å. An interesting feature of this complex is the absence of symmetry due to a pedestal (16 Å in height) at the base of the stalk, which makes the complex itself asymmetric (Figure 1). Eventually, to identify any structural analogy between the SDBC 3D structure and the structures of the main S-layer proteins from other species (Baranova et al., 2012; Bharat et al., 2017), we attempted comparative studies that further confirmed the very low sequence identity among S-layer proteins (data not shown).

The SDBC is integrated into the S-layer organization

Next, to attempt the *in situ* localization of the SDBC, we exploited the typical paracrystallinity of the S-layer as easily appreciable in

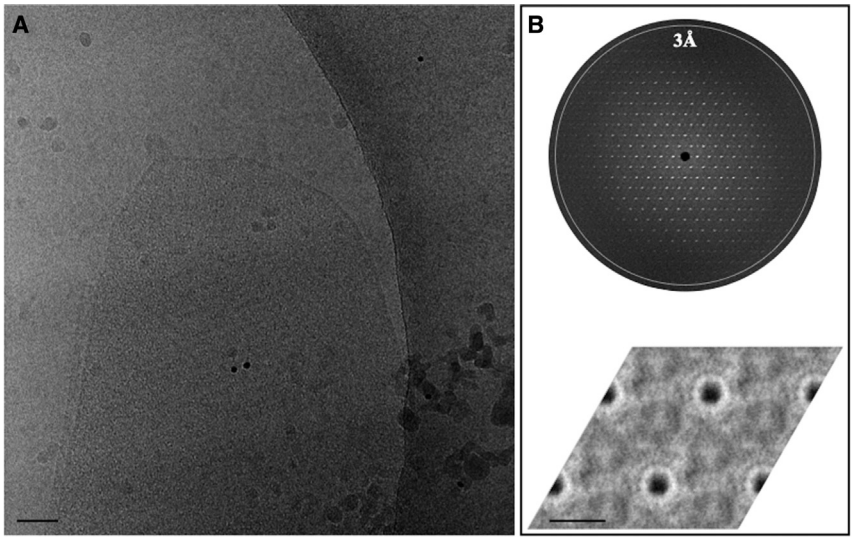

Figure 2. A cell-wall patch, its diffraction pattern, and related 2D map

The image shows a typical cell-wall patch, its characteristic regularity, and electron diffraction properties that are used to obtain a 2D electron density map. The image in (A) is a cryo-EM micrograph of a cell wall patch showing a regular pattern of stripes. Scale bar, 50 nm. The top image in (B) is the electron diffraction pattern of the patch shown in A. The white ring shows the diffraction limit having spots, hence retrievable structural information, beyond 3-Å resolution; this diffraction pattern is used to retrieve the 2D map (B – bottom image) with no symmetry imposed (p1). The scale bar in the 2D map is 100 Å.

the cryo-micrographs of cell-wall samples (Figure 2A). The intact cell walls, pretreated with lysozyme, were tested for their diffraction properties and analyzed by cryo-EC. The cell-wall patches were surprisingly ordered, showing regular and sharp diffraction spots beyond 3 Å (Figure 2B). Diffraction analysis on single movies resulted in two-dimensional (2D) maps that, with no imposed symmetry, showed a clear six-fold symmetry as previously reported (Figure 2B) (Baumeister et al., 1982; Farci et al., 2014). These analyses were performed on several tenths of membrane patches, all of which were found to occur with the same pattern and structure shown in Figure 2. The stratification integrity of the cell wall for each patch was further confirmed by cryo-electron tomography, allowing us to study only the patches with both outer and inner membranes preserved (Figure 3; Videos S1 and S2).

Given the previous findings for this S-layer (Baumeister et al., 1982) and the preliminary analysis shown in Figure 2, the data from the six best images were merged. The phase residuals of the merged images after lattice unbending and transfer function correction indicated significant information up to a resolution of 4.5 Å (Table 1) with crystals carrying a p6 symmetry and yielding the projection map shown in Figure 4. The projection map showed considerably more and unknown features than previously observed (Baumeister et al., 1982; Müller et al., 1996). An interesting feature of this S-layer is six complexes that connect each pore with another six neighboring pores (Figure 4). This unknown complex, with dimensions of 52 × 62 Å, shows a typical dihedral symmetry and might consist of oligomers of the S-layer protein DR_2508 (HPI), which was previously localized on the top side of this cell wall (Baumeister et al., 1982; Rachel et al., 1986). The pore region consists of a dome-like structure with diameters at the base and at the plateau of 145 Å and 98 Å, respectively. The plateau has a 45-Å diameter pore. The rest of the surface is covered by six repeated regions surrounding the pore, loyal to its p6 symmetry. Each of these regions is characterized by its own three-fold symmetry and shows the characteristic triangular shape of the SDBC with weaker densities at their center identifying the three comma-shaped pores of the complex. As observed by comparing the 2D projection maps and the SDBC 3D model, the dimensions (105 Å side length) and features of this region are coincident, confirming their correspondence. As evidenced in Figure 1, the stalk is located at the center of the SDBC and

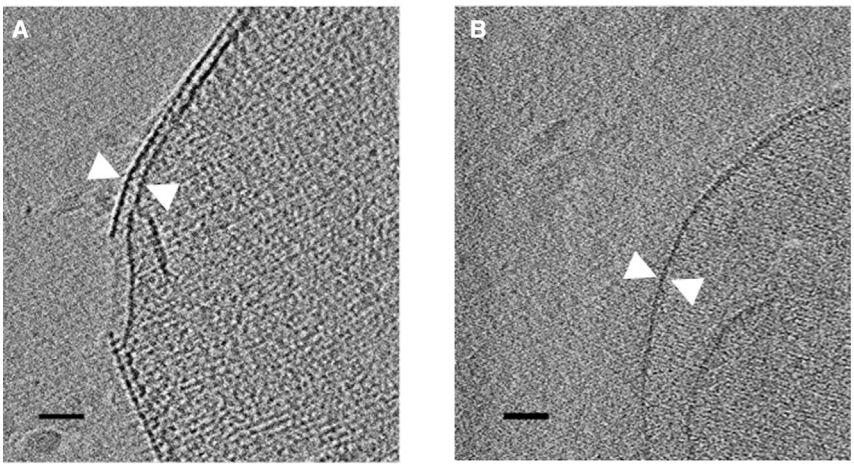

Figure 3. Thickness of an intact cell-wall patch

Patch integrity can be easily probed by cryo-electron tomography. Intact patches show a well-defined thickness and two clear membrane layers (A), while the absence of integrity appears clear in disrupted cell-wall fragments where only one membrane layer is visible (B). White arrowheads indicate the membrane thickness. Scale bars, 50 nm.

Table 1. Electron crystallographic image statistics and main image parameters

Plane group symmetry		p6
Unit cell parameters		
a (Å)		119.9 ± 0.3
b (Å)		192.2 ± 0.8
γ (°)		192.1 ± 1.4
No. of images		6
Range of defocus (Å)		39,500–120,021
Magnification		21,930×
Resolution (Å)	No. of unique reflections[a]	Phase residual (°)[b]
14.3	72	31.4
10.1	54	43.0
8.2	29	40.0
7.1	28	36.8
6.4	15	42.1
5.8	13	41.2
5.4	11	51.2
5.0	15	33.9
4.7	7	27.6
4.5	11	53.4

[a]With 1 ≤ IQ ≤ 6 to 4.5 Å.
[b]Amplitude-weighted, vectorial averaged phase residuals that show the phase deviation from theoretical 0°/180° (45° is random).

appears in orthogonal continuity with the three septa that merge by coiling up into a triple-spiral structure. Consistent with this, the 2D projection map also provides some hints about the SDBC orientation. In particular, specific features such as the comma-shaped pores and the facies at the center of the particle, different for each side, allow the SDBC to fit as oriented with the stalk toward the intracellular space (Figure 4). These analyses showed a clear *in situ* correspondence between the SDBC top views and specific areas of the S-layer units on the cell wall.

The SDBC functional integrity is confirmed by its gating properties and stepwise conductance increase

Finally, considering that the SDBC has peculiar porin-like properties (Farci et al., 2020) as also suggested here by the structural analysis, we assessed the functional integrity of the SDBC samples, obtained here by an improved isolation protocol. Conventional single-channel electrophysiology and reversal potential measurements confirmed previous observations (Farci et al., 2020), with the SDBC complex showing a single conductance unit (G) equal to 0.25 nS at 100 mM KCl and a stepwise multiple increase associated with insertion of more SDBC units (Figure 5A). The reversal potential value (V_{rev}) of SDBC in the presence of a KCl gradient of 0.1:0.5 M is +10 ± 3 mV, and the related permeability ratio was found to be PK^+/PCl^- = 1:0.65 (Figure 5B), confirming that the SDBC is a rather non-selective channel.

DISCUSSION

S-layers are proteinaceous paracrystalline structures composed by repeated units that surround the cells of many bacterial species. In several species, these structures are reported to disappear after a few generations of growth under optimal conditions, such as in research laboratories or bacterial factories, and the same behavior is expected to occur in ideal natural environments. However, S-layers are also reported to be stable structures for many species, even under optimal growth conditions. This is particularly true for extremophiles such as, for example, the most representative species in the *Thermus-Deinococcus* genus. The aforementioned aspects seem to candidate S-layers to the primary role of protection. Nonetheless, their persistence in extremophiles growing under mild conditions, hence in absence of stress factors, suggests a possible dual function whereby the one of protection coexists with one or more advantageous for the occupied niches, such as cell adhesion, salt nucleation, and others that at the moment might be ignored. The case of *D. radiodurans* and its S-layer is emblematic. This structure is reported to actively contribute to providing resistance under extreme conditions of desiccation and constant UV light irradiation, but the S-layer is not lost when these extreme conditions are absent over generations. Importantly, the S-layer represents not less than 15%–20% of the total protein content of a cell (Sleytr et al., 1993), so to express its components and keep the assembly machinery represents a huge effort in energy and resources. The reasons to retain these structures even under optimal conditions could depend on the synergy between structural and functional features of a given S-layer and/or on the degree of specialization reached by the extremophile. The *Thermus-Deinococcus* genus fits very well into this scheme; in fact, *Deinococcus* species are frequently specialized in resisting UV radiation and desiccation conditions and, especially in *D. radiodurans*, this resistance was strongly associated with S-layer integrity (Farci et al., 2016, 2018; Rothfuss et al., 2006). In this case, even in the absence of the stressing factor, the loss of the main S-layer protein would destabilize the extended complexity of this S-layer and the membranes below. In the same genus, the *Thermus* species not only are expected to have a similar complicated organization of their S-layers but also optimized their metabolism to high temperatures so that the source of stress became actually optimal and resulted in a factor of selection for optimum growth (Cava et al., 2009; Li et al., 2010). In this last case, the high temperature became a normal condition that is needed for the bacterium to grow, while in the previous example the presence of UV and desiccation did not became a specific need for growth but most likely resulted from a phylogenetic profile whereby ancestors might have adapted to grow in a constant UV background (e.g., prior to the geological oxygen crisis) (Farci et al., 2018; Ott et al., 2019a, 2019b). Contrary to the aforementioned S-layer types, it must be considered that many bacteria have an S-layer built by one or few proteins limited to a single peripheral surface layer; in this case, the S-layer might be easily lost in the absence of the stressing condition without negative effects on cell integrity.

D. radiodurans does not lose the S-layer during growth in the absence of stress factors (exposure to UV light and/or desiccation), suggesting that the S-layer units' functions might be connected to one or more of the layers below, and its loss would cause an extended destabilization of the entire cell wall. Similar indirect observations were reported previously (Farci et al., 2016, 2018; Rothfuss et al., 2006), but in the present work

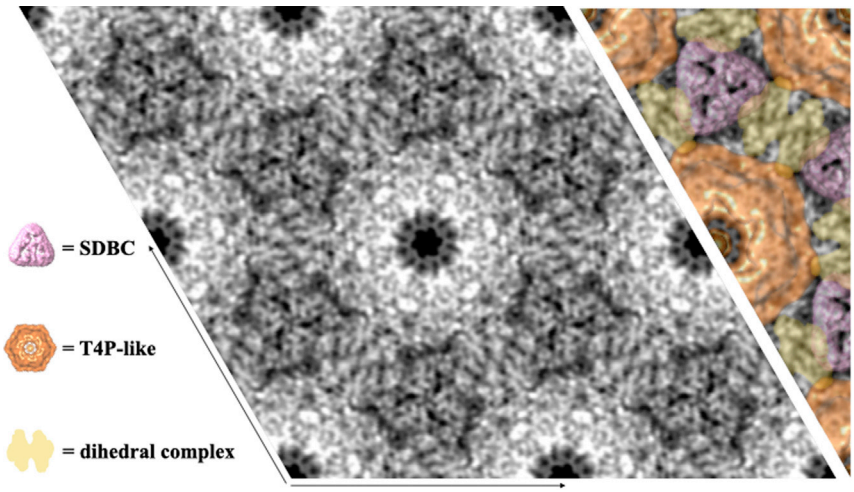

Figure 4. S-layer projection map, SDBC fitting, and localization of complexes

Projection map of the S-layer with imposed p6 symmetry at 4.5-Å resolution from six averaged images showing a unit cell of 192 × 192 Å (black arrows). At the center of the map is located the pore region, which identifies the type IV-like piliation system, surrounded by six interpore regions with three-fold symmetry, which coincide with the SDBC. Between those two regions and above them is located a third unknown complex with a typical dihedral symmetry. The colored part of the image shows the type IV-like piliation system in orange, the SDBC in pink, and the dihedral complex in yellow, eventually identifying their relative positions.

the SDBC's features provided structural evidence for this extension, corroborating the reported functional ones (Farci et al., 2020).

In the present work, the low-resolution 3D structure of the SDBC and the middle- to high-resolution 2D map of intact cell walls allowed us not only to infer the SDBC *in situ* localization and orientation but also to demonstrate the interaction between the S-layer and the underlying membrane. In fact, the stalk region of the SDBC particle was found to be extended for 72 Å toward the intracellular space constraining the order extension to the layers below, crossing the outer membrane and reaching the periplasm at least, bypassing the porin "sieving" system of the outer membrane (Vergalli et al., 2020). Moreover, this structural function is expected to be extended to the main body of the particle that, considering its porin-like properties (Farci et al., 2020), must be partially embedded in the outer membrane, allowing a controlled structural and functional continuity between the periplasm and the extracellular space. In this respect, the pedestal region must play an essential role in the interaction with the membrane as well as in the stabilization of the stalk extension. Furthermore, the 2D cryo-EC map allowed us to conclude not only that the S-layer in this bacterium is composed of two other protein complexes but also to visualize them for the first time, showing the supramolecular organization of this S-layer. Results reported here highlight the peculiarities of this specific S-layer: (1) instead of being the paracrystalline repetition of the same protein, this structure is composed of three different protein complexes; (2) its main protein complex, the SDBC, is composed of six different subunits; and (3) it has 3D structural shape and dimensions very distinct from any other known S-layer complex reported (Baranova et al., 2012; Bharat et al., 2017). These results are the bases for future studies to better disclose the integrated structural/functional roles of the SDBC, a complex necessary not only for gating and protection but also as a building unit for the whole cell wall. Considering that the SDBC represents the main S-layer unit, it becomes evident how much the regularity and the stability of the outer membrane is influenced by its presence. This work confirms the pivotal role of S-layers as protective and stabilizing structures with functionalized units specializing in protection and interaction with the environment.

STAR★METHODS

Detailed methods are provided in the online version of this paper and include the following:

- KEY RESOURCES TABLE
- RESOURCE AVAILABILITY
  - Lead contact
  - Materials availability
  - Data and code availability

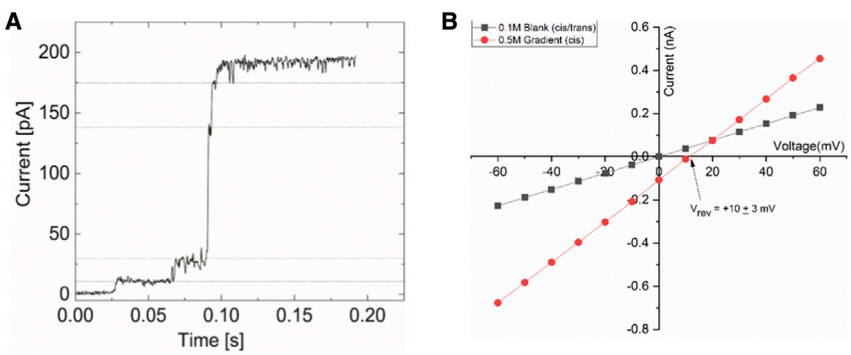

Figure 5. SDBC functionality assays

(A) Upon stepwise insertions at 100 mM KCl (pH 7.0), the ion current increases (black trace) indicating a new SDBC insertion. A single SDBC contributes with a conductance unit (G) equal to 0.25 nS.

(B) Reversal potential plot of SDBC channels in potassium chloride showing a V_{rev} of +10 ± 3 mV. The signals are filtered at 1,000 Hz. Measurements and fitting were performed according to Farci et al. (2020).

- EXPERIMENTAL MODEL AND SUBJECT DETAILS
  - Cell lines
- METHOD DETAILS
  - Cell walls isolation
  - SDBC purification
  - Electron microscopy
  - Electrophysiology assay
- QUANTIFICATION AND STATISTICAL ANALYSIS
- ADDITIONAL RESOURCES

SUPPLEMENTAL INFORMATION

Supplemental information can be found online at https://doi.org/10.1016/j.str.2021.06.014.

ACKNOWLEDGMENTS

This work was supported by the National Science Centre (Poland) with the Sonata BIS 7 Program (2017) grant PRO-2017/26/E/NZ1/00344 and the Harmonia 10 Program (2018) grant PRO-2018/30/M/NZ1/00284 (both to D.P., D.F., and P.H.), and the Czech Science Foundation grant 1825144Y (to S.K.). Cryo-EM data collection was performed at the core facility Cryo-Electron Microscopy and Tomography, CEITEC, Brno, Czech Republic.

AUTHOR CONTRIBUTIONS

Conceptualization, D.P. and D.F.; methodology, D.P. and D.F.; validation, D.P., D.F., S.K.; M.W., M.C., and I.V.B.; formal analysis, D.P., D.F., S.K., S.P., M.W., M.C., and I.V.B.; investigation, D.P., D.F., S.K., S.P., P.H., M.C., and I.V.B.; resources, D.P. and D.F.; data curation, D.P. and D.F.; writing – original draft, D.P., D.F., S.K., P.H., S.P., M.W., M.C., and I.V.B.; writing – review & editing, D.P. and D.F.; visualization, D.P., D.F., and S.P.; supervision, D.P.; project administration, D.P. and D.F.; funding acquisition, D.P. and S.K.

DECLARATION OF INTERESTS

The authors declare no competing interests.

INCLUSION AND DIVERSITY

While citing references scientifically relevant for this work, we actively worked to promote gender balance in our reference list. The author list of this paper includes contributors from the location where the research was conducted who participated in the data collection, design, analysis, and/or interpretation of the work.

Received: February 9, 2021
Revised: May 22, 2021
Accepted: June 25, 2021
Published: July 14, 2021

REFERENCES

Adamec, F., Farci, D., Bína, D., Litvín, R., Khan, T., Fuciman, M., Piano, D., and Polívka, T. (2020). Photophysics of deinoxanthin, the keto-carotenoid bound to the main S-layer unit of *Deinococcus radiodurans*. Photochem. Photobiol. Sci. *19*, 495–503. https://doi.org/10.1039/d0pp00031k.

Anderson, A.W., Nordan, H.C., Cain, R.F., Parrish, G., and Duggan, D. (1956). Studies on a radio-resistant micrococcus. I. Isolation, morphology, cultural characteristics, and resistance to gamma radiation. Food Technol. *10*, 575–577.

Bahl, H., Scholz, H., Bayan, N., Chami, M., Leblon, G., Gulik-Krzywicki, T., Shechter, E., Fouet, A., Mesnage, S., Tosi-Couture, E., et al. (1997). Molecular biology of S-layers. FEMS Microbiol. Rev. *20*, 47–98. https://doi.org/10.1111/j.1574-6976.1997.tb00304.x.

Baranova, E., Fronzes, R., Garcia-Pino, A., Van Gerven, N., Papapostolou, D., Péhau-Arnaudet, G., Pardon, E., Steyaert, J., Howorka, S., and Remaut, H. (2012). SbsB structure and lattice reconstruction unveil Ca^{2+} triggered S-layer assembly. Nature *487*, 119–122. https://doi.org/10.1038/nature11155.

Baumeister, W., Karrenberg, F., Rachel, R., Engel, A., ten Heggeler, B., and Saxton, W.O. (1982). The major cell envelope protein of *Micrococcus radiodurans* (*R1*). *Structural and chemical characterization*. Eur. J. Biochem. *125*, 535–544. https://doi.org/10.1111/j.1432-1033.1982.tb06715.x.

Baumeister, W., Barth, M., Hegerl, R., Guckenberger, R., Hahn, M., and Saxton, W.O. (1986). Three-dimensional structure of the regular surface layer (HPI layer) of *Deinococcus radiodurans*. J. Mol. Biol. *187*, 241–250. https://doi.org/10.1016/0022-2836(86)90231-7.

Beckers, M., and Sachse, C. (2020). Permutation testing of Fourier shell correlation for resolution estimation of cryo-EM maps. J. Struct. Biol. *212*, 107579. https://doi.org/10.1016/j.jsb.2020.107579.

Beveridge, T.J., Pouwels, P.H., Sára, M., Kotiranta, A., Lounatmaa, K., Kari, K., Kerosuo, E., Haapasalo, M., Egelseer, E.M., Schocher, I., et al. (1997). Functions of S-layers. FEMS Microbiol. Rev. *20*, 99–149. https://doi.org/10.1111/j.1574-6976.1997.tb00305.x.

Bharat, T.A.M., Kureisaite-Ciziene, D., Hardy, G.G., Yu, E.W., Devant, J.M., Hagen, W.J.H., Brun, Y.V., Briggs, J.A.G., and Löwe, J. (2017). Structure of the hexagonal surface layer on *Caulobacter crescentus* cells. Nat. Microbiol. *2*, 17059. https://doi.org/10.1038/nmicrobiol.2017.59.

Biyani, N., Righetto, R.D., McLeod, R., Caujolle-Bert, D., Castano-Diez, D., Goldie, K.N., and Stahlberg, H. (2017). Focus: the interface between data collection and data processing in cryo-EM. J. Struct. Biol. *198*, 124–133. https://doi.org/10.1016/j.jsb.2017.03.007.

Cava, F., Hidalgo, A., and Berenguer, J. (2009). *Thermus thermophilus* as biological model. Extremophiles *13*, 213–231. https://doi.org/10.1007/s00792-009-0226-6.

Fagan, R.P., and Fairweather, N.F. (2014). Biogenesis and functions of bacterial S-layers. Nat. Rev. Microbiol. *12*, 211–222. https://doi.org/10.1038/nrmicro3213.

Farci, D., Bowler, M.W., Kirkpatrick, J., McSweeney, S., Tramontano, E., and Piano, D. (2014). New features of the cell wall of the radio-resistant bacterium *Deinococcus radiodurans*. Biochim. Biophys. Acta *1838*, 1978–1984. https://doi.org/10.1016/j.bbamem.2014.02.014.

Farci, D., Bowler, M.W., Esposito, F., McSweeney, S., Tramontano, E., and Piano, D. (2015). Purification and characterization of DR_2577 (SlpA) a major S-layer protein from *Deinococcus radiodurans*. Front. Microbiol. *6*, 414. https://doi.org/10.3389/fmicb.2015.00414.

Farci, D., Slavov, C., Tramontano, E., and Piano, D. (2016). The S-layer protein DR_2577 binds the carotenoid deinoxanthin and under desiccation conditions protect against UV-radiation in *Deinococcus radiodurans*. Front. Microbiol. *7*, 155. https://doi.org/10.3389/fmicb.2016.00155.

Farci, D., Esposito, F., El Alaoui, S., and Piano, D. (2017). S-layer proteins as a source of carotenoids: isolation of the carotenoid cofactor deinoxanthin from its S-layer protein DR_2577. Food Res. Int. *99*, 868–876. https://doi.org/10.1016/j.foodres.2016.10.003.

Farci, D., Slavov, C., and Piano, D. (2018). Coexisting properties of thermostability and Ultraviolet radiation resistance in the main S-layer complex of *Deinococcus radiodurans*. Photochem. Photobiol. Sci. *17*, 81–88. https://doi.org/10.1039/c7pp00240h.

Farci, D., Guadalupi, G., Bierła, K., Lobinski, R., and Piano, D. (2019). The role of iron and copper on the oligomerization dynamics of DR_2577, the main S-layer protein of *Deinococcus radiodurans*. Front. Microbiol. *10*, 1450. https://doi.org/10.3389/fmicb.2019.01450.

Farci, D., Aksoyoglu, M.A., Farci, S.F., Bafna, J.A., Bodrenko, I., Ceccarelli, M., Kirkpatrick, J., Winterhalter, M., Kereïche, S., and Piano, D. (2020). Structural insights into the main S-layer unit of *Deinococcus radiodurans* reveal a massive protein complex with porin-like features. J. Biol. Chem. *295*, 4224–4236. https://doi.org/10.1074/jbc.RA119.012174.

Gentner, N.E., and Mitchel, R.E. (1975). Ionizing radiation-induced release of a cell surface nuclease from *Micrococcus radiodurans*. Radiat. Res. *61*, 204–215.

Gipson, B., Zeng, X., Zhang, Z.Y., and Stahlberg, H. (2007). 2dx—user-friendly image processing for 2D crystals. J. Struct. Biol. *157*, 64–72. https://doi.org/10.1016/j.jsb.2006.07.020.

Hall, S.R., Shenton, W., Engelhardt, H., and Mann, S. (2001). Site-specific organization of gold nanoparticles by biomolecular templating. Chemphyschem *2*, 184–186. https://doi.org/10.1002/1439-7641(20010316)2:3<184::AID-CPHC184>3.0.CO;2-J.

Harauz, G., and van Heel, M. (1986). Exact filters for general geometry three dimensional reconstruction. Optik *73*, 146–156.

Kumar, J., Ghosh, P., and Kumar, A. (2021). Ultraviolet-B radiation stress-induced toxicity and alterations in proteome of *Deinococcus radiodurans*. Microb. Physiol. *31*, 1–15. https://doi.org/10.1159/000512018.

Li, H., Ji, X., Zhou, Z., Wang, Y., and Zhang, X. (2010). *Thermus thermophilus* proteins that are differentially expressed in response to growth temperature and their implication in thermoadaptation. J. Proteome Res. *9*, 855–864. https://doi.org/10.1021/pr900754y.

Li, X., Mooney, P., Zheng, S., Booth, C.R., Braunfeld, M.B., Gubbens, S., Agard, D.A., and Cheng, Y. (2013). Electron counting and beam-induced motion correction enable near-atomic-resolution single-particle cryo-EM. Nat. Methods *10*, 584–590. https://doi.org/10.1038/nmeth.2472.

Lim, S., Jung, J.H., Blanchard, L., and de Groot, A. (2019). Conservation and diversity of radiation and oxidative stress resistance mechanisms in *Deinococcus* species. FEMS Microbiol. Rev. *43*, 19–52. https://doi.org/10.1093/femsre/fuy037.

Lister, T.E., and Pinhero, P.J. (2001). *In vivo* atomic force microscopy of surface proteins on *Deinococcus radiodurans*. Langmuir *17*, 2624–2628.

Mark, S.S., Bergkvist, M., Yang, X., Teixeira, L.M., Bhatnagar, P., Angert, E.R., and Batt, C.A. (2006). Bionanofabrication of metallic and semiconductor nanoparticle arrays using S-layer protein lattices with different lateral spacings and geometries. Langmuir *22*, 3763–3774. https://doi.org/10.1021/la053115v.

Mastronarde, D.N. (2005). Automated electron microscope tomography using robust prediction of specimen movements. J. Struct. Biol. *152*, 36–51. https://doi.org/10.1016/j.jsb.2005.07.007.

Messner, P., and Sleytr, U.B. (1991). Bacterial surface layer glycoproteins. Glycobiology *1*, 545–551. https://doi.org/10.1093/glycob/1.6.545.

Messner, P., Allmaier, G., Schäffer, C., Wugeditsch, T., Lortal, S., König, H., Niemetz, R., and Dorner, M. (1997). Biochemistry of S-layers. FEMS Microbiol. Rev. *20*, 25–46. https://doi.org/10.1111/j.1574-6976.1997.tb00303.x.

Mindell, J.A., and Grigorieff, N. (2003). Accurate determination of local defocus and specimen tilt in electron microscopy. J. Struct. Biol. *142*, 334–347. https://doi.org/10.1016/s1047-8477(03)00069-8.

Müller, D.J., Baumeister, W., and Engel, A. (1996). Conformational change of the hexagonally packed intermediate layer of *Deinococcus radiodurans* monitored by atomic force microscopy. J. Bacteriol. *178*, 3025–3303. https://doi.org/10.1128/jb.178.11.3025-3030.1996.

Müller, D.J., Schoenenberger, C.A., Schabert, F., and Engel, A. (1997). Structural changes in native membrane proteins monitored at subnanometer resolution with the atomic force microscope: a review. J. Struct. Biol. *119*, 149–157. https://doi.org/10.1006/jsbi.1997.3878.

Ott, E., Kawaguchi, Y., Özgen, N., Yamagishi, A., Rabbow, E., Rettberg, P., Weckwerth, W., and Milojevic, T. (2019a). Proteomic and metabolomic profiling of *Deinococcus radiodurans* recovering after exposure to simulated low Earth orbit vacuum conditions. Front. Microbiol. *10*, 909. https://doi.org/10.3389/fmicb.2019.00909.

Ott, E., Fuchs, F.M., Moeller, R., Hemmersbach, R., Kawaguchi, Y., Yamagishi, A., Weckwerth, W., and Milojevic, T. (2019b). Molecular response of *Deinococcus radiodurans* to simulated microgravity explored by proteometabolomic approach. Sci. Rep. *9*, 18462. https://doi.org/10.1038/s41598-019-54742-6.

Pavkov, T., Egelseer, E.M., Tesarz, M., Svergun, D.I., Sleytr, U.B., and Keller, W. (2008). The structure and binding behavior of the bacterial cell surface layer protein SbsC. Structure *16*, 1226–1237. https://doi.org/10.1016/j.str.2008.05.012.

Pavkov-Keller, T., Howorka, S., and Keller, W. (2011). The structure of bacterial S-layer proteins. Prog. Mol. Biol. Transl. Sci. *103*, 73–130. https://doi.org/10.1016/B978-0-12-415906-8.00004-2.

Penczek, P.A. (2010). Resolution measures in molecular electron microscopy. Methods Enzymol. *482*, 73–100. https://doi.org/10.1016/S0076-6879(10)82003-8.

Peters, J., and Baumeister, W. (1986). Molecular cloning, expression, and characterization of the gene for the surface (HPI)-layer protein of *Deinococcus radiodurans* in *Escherichia coli*. J. Bacteriol. *167*, 1048–1054. https://doi.org/10.1128/jb.167.3.1048-1054.1986.

Pettersen, E.F., Goddard, T.D., Huang, C.C., Couch, G.S., Greenblatt, D.M., Meng, E.C., and Ferrin, T.E. (2004). UCSF Chimera—a visualization system for exploratory research and analysis. J. Comput. Chem. *25*, 1605–1612. https://doi.org/10.1002/jcc.20084.

Pum, D., Toca-Herrera, J.L., and Sleytr, U.B. (2013). S-layer protein self-assembly. Int. J. Mol. Sci. *14*, 2484–2501. https://doi.org/10.3390/ijms14022484.

Rachel, R., Pum, D., Šmarda, J., Šmajs, D., Komrska, J., Krzyzánek, V., Rieger, G., and Stetter, K.O. (1997). Fine structure of S-layers. FEMS Microbiol. Rev. *20*, 13–23.

Rachel, R., Jakubowski, U., Tietz, H., Hegerl, R., and Baumeister, W. (1986). Projected structure of the surface protein of *Deinococcus radiodurans* determined to 8 Å resolution by cryomicroscopy. Ultramicroscopy *20*, 305–316.

Rothfuss, H., Lara, J.C., Schmid, A.K., and Lidstrom, M.E. (2006). Involvement of the S-layer proteins Hpi and SlpA in the maintenance of cell envelope integrity in *Deinococcus radiodurans* R1. Microbiology *152*, 2779–2787. https://doi.org/10.1099/mic.0.28971-0.

Sára, M., and Sleytr, U.B. (2000). S-layer proteins. J. Bacteriol. *182*, 859–868. https://doi.org/10.1128/JB.182.4.859-868.2000.

Scheres, S.H. (2012). RELION: implementation of a Bayesian approach to cryo-EM structure determination. J. Struct. Biol. *180*, 519–530. https://doi.org/10.1016/j.jsb.2012.09.006.

Scheres, S.H., and Chen, S. (2012). Prevention of overfitting in cryo-EM structure determination. Nat. Methods *9*, 853–854. https://doi.org/10.1038/nmeth.2115.

Sleytr, U.B., and Glauert, A.M. (1975). Analysis of regular arrays of subunits on bacterial surfaces: evidence for a dynamic process of assembly. J. Ultrastruct. Res. *50*, 103–116. https://doi.org/10.1016/s0022-5320(75)90012-x.

Sleytr, U.B. (1978). Regular arrays of macromolecules on bacterial cell walls: structure, chemistry, assembly, and function. Int. Rev. Cytol. *53*, 1–62. https://doi.org/10.1016/s0074-7696(08)62240-8.

Sleytr, U.B., Messner, P., Pum, D., and Sára, M. (1993). Crystalline bacterial cell surface layers. Mol. Microbiol. *10*, 911–916. https://doi.org/10.1111/j.1365-2958.1993.tb00962.x.

Sleytr, U.B., and Sàra, M. (1997). Bacterial and archaeal S-layer proteins: structure–function relationship and their biotechnological applications. Trends Biotechnol. *15*, 20–26. https://doi.org/10.1016/S0167-7799(96)10063-9.

Tang, G., Peng, L., Baldwin, P.R., Mann, D.S., Jiang, W., Rees, I., and Ludtke, S.J. (2007). EMAN2: an extensible image processing suite for electron microscopy. J. Struct. Biol. *157*, 38–46. https://doi.org/10.1016/j.jsb.2006.05.009.

Vergalli, J., Bodrenko, I.V., Masi, M., Moynié, L., Acosta-Gutiérrez, S., Naismith, J.H., Davin-Regli, A., Ceccarelli, M., van den Berg, B., Winterhalter, M., and Pagès, J.M. (2020). Porins and small-molecule translocation across the outer membrane of Gram-negative bacteria. Nat. Rev. Microbiol. *18*, 164–176. https://doi.org/10.1038/s41579-019-0294-2.

Zhang, K. (2016). Gctf: real-time CTF determination and correction. J. Struct. Biol. *193*, 1–12. https://doi.org/10.1016/j.jsb.2015.11.003.

Zheng, S.Q., Palovcak, E., Armache, J.P., Verba, K.A., Cheng, Y., and Agard, D.A. (2017). MotionCor2: anisotropic correction of beam-induced motion for improved cryo-electron microscopy. Nat. Methods *14*, 331–332. https://doi.org/10.1038/nmeth.4193.

STAR★METHODS

KEY RESOURCES TABLE

REAGENT or RESOURCE	SOURCE	IDENTIFIER
Bacterial and virus strains		
Deinococcus radiodurans R1	ATCC (https://www.atcc.org/)	ATCC 13939
Chemicals, peptides, and recombinant proteins		
Tryptone	Becton, Dickinson and Company	Cat# 211705
Yeast extract	Becton, Dickinson and Company	Cat# 212750
Glucose	Carlo Erba	CAS n° 50-99-7
Sodium Phosphate dibasic dodecahydrate	Carlo Erba	CAS n° 10039-32-4
Sodium Phosphate mobasic monohydrate	Carlo Erba	CAS n° 10049-21-5
DNase	Roche	CAS n°
Lysozyme	Sigma Aldrich	CAS n° 12650-88-3
Bradford assay kit	ThermoFisher	Cat# 23246
n-dodecyl-β-D-maltoside	Glycon	Cat# D97002-C
Sodium chloride	Sigma Aldrich	CAS n° 7647-14-5
DPhPC	Avanti Polar Lipids	Cat# 860337P-1MG
Potassium chloride	Carlo Erba	CAS n° 7447-40-7
HEPES	Roth	CAS n° 7365-45-9
Deposited data		
cryo-EM map of the SDBC	This study	EMDB-12169
Software and algorithms		
dosefgpu_driftcorr	Li et al., 2013	https://github.com/jianglab/motioncorr/blob/master/Readme.txt
CTFFIND3	Mindell and Grigorieff, 2003	https://grigoriefflab.umassmed.edu/ctf_estimation_ctffind_ctftilt
GCTF	Zhang, 2016	https://www2.mrc-lmb.cam.ac.uk/research/locally-developed-software/zhang-software/
EMAN2	Tang et al., 2007	https://blake.bcm.edu/emanwiki/EMAN2
RELION 3.1 beta	Scheres, 2012	https://github.com/3dem/relion
MotionCor2	Zheng et al., 2017	https://emcore.ucsf.edu/ucsf-software
Focus package	Biyani et al., 2017	https://lbem-focus.epfl.ch/about.php
2*dx* package	Gipson et al., 2007	https://www.c-cina.org/stahlberg/research/tools/soft/2dx/
Chimera	Pettersen et al., 2004	https://www.cgl.ucsf.edu/chimera/
Etomo	Mastronarde, 2005	https://bio3d.colorado.edu/imod/
Other		
anion-exchange chromatography column	Hiload HP, Amersham	n.a.
Quantifoil R2/1.3 holey carbon grids	Quantifoil	n.a.
Autogrid	FEI, Eindhoven, Netherlands	n.a.

RESOURCE AVAILABILITY

Lead contact

Further information should be directed to and will be fulfilled by the lead contact, Dr. Dario Piano (dario.piano@unica.it).

Materials availability

Primary data are available upon reasonable request to the lead contact.

Data and code availability

The final 3D volume of the SDBC, FSC data, and other relevant information about data acquisition and processing have been deposited in the Electron Microscopy Data Bank, EMDB-12169. All data will be released upon publication. This paper does not report original code. Any additional information required to reanalyze the data reported in this paper is available from the lead contact upon request.

EXPERIMENTAL MODEL AND SUBJECT DETAILS

Cell lines

Deinococcus radiodurans cultures (strain R1; ATCC 13939) were cultivated in Tryptone Glucose Yeast extract broth (TGY) at 30°C for 24 h, as describe in (Farci et al., 2014).

METHOD DETAILS

Cell walls isolation

Cell walls were isolated at 4°C in dim light as describe in (Farci et al., 2014) with several modifications. Briefly, cells were harvested by centrifugation at 5000 g for 10 min, then resuspended in a buffer containing 50 mM sodium phosphate, pH 7.8 (buffer A) and supplemented with DNase. Cells were disrupted using a French Pressure Cell (3 cycles at 1100 psi). The homogenate was centrifuged two times for 10 min at 2000 g to remove the debris, then ultracentrifuged at 48,000 g for 10 min. The final pink pellet was resuspended in buffer A and incubated for 8 hr with 100 μg/mL lysozyme under gentle shaking (800 rpm) at 30°C, to remove surface polysaccharides. Digested cell wall fragments were pelleted by centrifugation at 48,000 g for 10 min at 4°C, washed three times with buffer A and resuspended in a small volume of buffer A. Resuspended samples were used for the cryo-electron crystallography and tomography.

SDBC purification

SDBC purification was performed following the procedure reported in (Farci et al., 2020). Briefly, the total protein concentration of the cell walls fragments suspension was estimated by a commercial Bradford assay kit (ThermoFisher) and was adjusted to a concentration of 3-5 mg/mL. The resuspension was finally solubilised for 3-4 hr at room temperature by using 10% (w/v) n-dodecyl-β-D-maltoside (β-DDM) to reach a final concentration of 1.4% and 0.5–0.7 mg/mL of total proteins. Solubilized membranes were centrifuge at 48,000 g for 10 min at 10°C and the supernatant was applied onto a pre-equilibrated anion-exchange chromatography column (Hiload HP, Amersham) and subsequently subjected to buffer B (50 mM sodium phosphate, pH 7.4; 0.05% (w/v) β-DDM) at a flow rate of 0.5 mL/min. The SDBC applied to a Hiload HP column was washed with buffer B until the absorbance stayed stable for 2 columns volumes. Finally, isolated SDBC was eluted with a linear gradient of 0-2.5M NaCl in buffer C (50 mM sodium phosphate, pH 7.4; 2.5 M NaCl; 0.05% (w/v) β-DDM). In these studies, all chromatography columns were subjected to the ReGenFix procedure (https://www.regenfix.eu/) for regeneration and calibration prior use. Protein stability and deinoxanthin retention were assessed by absorption spectroscopy at room temperature (Farci et al., 2016). Absorption spectra were recorded in the 200-800 nm range using the presence of the ~495 nm band and the 495/280 nm ratio as an indicator of folded deinoxanthin (Farci et al., 2016).

Electron microscopy

Cryo-electron microscopy

The whole sample preparation and data acquisition was done at CEITEC, Brno, Czech Republic.

Quantifoil R2/1.3 holey carbon grids were glow-discharged prior use. Both, SDBC and cell wall patches samples were blotted and vitrified using a Vibrobot plunge-freezing machine (Mark IV, ThermoFisher) at room temperature (blot force 2, blotting time 2 s, 100% humidity), and placed in autogrid (FEI, Eindhoven, Netherlands) prior image acquisition.

For Single Particle Analysis, SDBC datasets were acquired with a FEI Arctica TEM (ThermoFisher) at an operating voltage of 200 kV with a FEI Falcon 3 4k×4k direct detection camera. Images were automatically recorded by the EPU software at a nominal magnification of 59,000×, yielding a final image pixel size of 0.96 Å. Image defocus was set in EPU to vary between −1 μm and −3.3 μm, the total electron dose used to acquire a single image was ~1.0 electrons/Å^2.

For cryo-electron tomography and crystallography, grids of cell wall patches were transferred to a Titan-Krios TEM (ThermoFisher) operating at 300 kV, and equipped with a Cs-corrector (cs 2.7 mm), a Quantum GIF energy filter (slit width set to 20eV), and a post-GIF K2 camera (Gatan) at a magnification corresponding to a pixel size of 2.28 Å/px (~21,000x). A dose-symmetric scheme (3° increment, range ±60°) was used for tomography acquisition by SerialEM software (Mastronarde, 2005). The defocus was set to vary between 2 μm and 5 μm.

Single particle analysis and cryo-electron crystallography processing

We collected 1573 micrographs for which CTF and ice quality was inspected. A total of 1554 micrographs were selected for further processing.

The *SDBC* frames were aligned and summed with the GPU-based dosefgpu_driftcorr (Li et al., 2013) program prior to further analysis. Image CTFs were estimated by CTFFIND3 (Mindell and Grigorieff, 2003) while the micrographs' resolution by the GCTF's EquiPhase Averaging (EPA) procedure (Zhang, 2016) by determining the local defocus for each particle and refining it for each single frame, finally improving the CTF parameters. A total of 11,086 particles were picked semi-automatically from 1310 micrographs using the e2boxer program from EMAN2 (Tang et al., 2007). The particles' coordinates were then converted and used in RELION 3.1 beta

(Scheres, 2012) to extract them with a box size of 512x512 pixels. The dataset was subject of 4 rounds of 2D classifications and subsequent selection of the classes of interest. A de novo initial 3D model was generated using a Stochastic Gradient Descent (SGD) algorithm from the 2D particles and used to run a 3D classification with 5 classes. The 3 best classes were selected, and another run of 3D classification was performed to check the consistency of the dataset. The best 3D model obtained after the 3D classification was subject to the 3D refine procedures. Briefly, the 3D auto-refinement procedure was performed by using the Fourier Shell Correlation (FSC) gold standard to prevent the overfitting in structure determination, and by estimating the accuracy of the angular assignments (Scheres and Chen, 2012). The resolution was estimated on the base of the Fourier Shell Correlation (FSC) calculated curves (Harauz and van Heel, 1986; Penczek, 2010; Beckers and Sachse, 2020).

For cryo-electron crystallography, 8-frames movies were drift corrected using MotionCor2 (Zheng et al., 2017) on the Focus package (Biyani et al., 2017). The resulting micrographs were processed on the same package but this time in 2D crystallography mode according to the latest implementations of the 2*dx* package (Gipson et al., 2007). Briefly, for each micrograph the Fast Fourier Transform (FFT), defocus, and astigmatism were calculated. The reciprocal lattice relative to the crystalline regions for each micrograph was determined from the calculated FFT by the algorithms FindLattice and GetLattice (Gipson et al., 2007). For each image, after applying the Constant Transfer Function (CTF) correction, a lattice's spot list was obtained followed by two cycles of unbending and a second CTF correction. Finally, a two-dimensional projection map relative to each image with no imposed symmetry (p1) was obtained (Gipson et al., 2007). Eventually, out of 42 processed micrographs, the best 6 best images were merged to obtain the final projection map by using the 2D merge suite from Focus also in 2D crystallography mode with imposed p6 symmetry (Biyani et al., 2017).

The 3D models' visualization and the fittings were done using the Chimera software (Pettersen et al., 2004). No previous structure was used for the analyses.

Cryo-electron tomography processing

More than 40 tomograms were processed by the *etomo* and IMOD software (Mastronarde, 2005). Tomograms were aligned using gold fiducial markers by weighted back-projection algorithms (Mastronarde, 2005). Only tomograms with minimal alignment errors (between 0.1 and 0.2 nm) were selected for the final reconstruction. No further filtering and/or contrast enhancement was performed. All analyses successfully reproduce the same results validating the data here presented. No previous structure was used for the analyses.

Electrophysiology assay

Conventional and reversal electrophysiology assays were performed according to (Farci et al., 2020). Briefly, bilayer lipid membranes were formed using DPhPC in a 100 μm diameter aperture of a two-compartment Teflon chamber (2.5 mL each) separated by a 25 μm thick Teflon partition. After pretreatment with a hexadecane/hexane solution (1% v/v) and 20 min of solvent evaporation, both chambers were filled with buffer solution (100 mM KCl, 10mM HEPES, pH 7.0) and 10 μL of lipids in pentane (5 mg/mL) were added on top allowing bilayers formation. Next, the SDBC sample was added into the *cis*-side of the chamber. The *cis* side of the chamber was considered the virtual ground. For conventional measurements, current traces records were acquired by Ag/AgCl electrodes. Reversal potential (V_{rev}) measurements were performed using calomel electrodes. Briefly, a current-voltage (*I-V*) recording of this multichannel state was captured by varying the V_m from +60 to −60 in decrements of ΔV_m = 5 mV and its profile was treated as the blank (no salt gradient). Subsequently, identical *I-V* measurements were performed while changing the salt concentration on one side of the membrane with Δ(Salt) = 500 mM. The reversal potential was determined by comparing this *I-V* profile with that of the blank. The V_{rev} was then fitted to *Goldman-Hodgkin-Katz* (GHK) Equation 1 where the selectivity of the channel is expressed as the ratio of the permeabilities of the anion and the cation (P_C/P_A).

$$E_m = \frac{RT}{F}\ln\left(\frac{\sum_i^n P_C[\mu_c]_o + \sum_j^m P_A[\mu_A]_i}{\sum_i^n P_C[\mu_c]_i + \sum_j^m P_A[\mu_A]_o}\right) \quad \text{(Equation 1)}$$

The Axopatch 200B (Molecular Devices, LLC) patch-clamp amplifier in V-clamp mode with a CV-203BU headstage was used. The output signal was filtered by a low-pass Bessel filter at 10 kHz and saved at a sampling frequency of 50 kHz using an Axon Digidata 1440A digitizer (Molecular Devices, LLC). For data acquisition and analysis, a homemade LabVIEW (National Instruments), Clampfit 10.0.3 (Molecular Devices, LLC), Origin Lab 2018 (Northampton, MA), Adobe Illustrator (v24.2.3), and python 3 were used.

QUANTIFICATION AND STATISTICAL ANALYSIS

SDBC and membrane isolation for data analyses was performed on more than 20 independent preparations. Micrographs, tomograms, projection maps, and electrophysiology assays are representative of at least three independent replicates. Electron crystallographic image statistics and main images parameters are indicated on Table 1. The calculation of Fourier Shell Correlation (FSC) curves for the single-particle analysis is reported in Figure S1. All attempts to reproduce the results here presented were successful.

ADDITIONAL RESOURCES

No additional resources are available.